Geometric charges and nonlinear elasticity of two-dimensional elastic metamaterials

Yohai Bar-Sinai (יוחאי בר-סיני)[a], Gabriele Librandi[a], Katia Bertoldi[a], and Michael Moshe (מיכאל משה)[b,1]

[a]School of Engineering and Applied Sciences, Harvard University, Cambridge, MA 02138; and [b]Racah Institute of Physics, The Hebrew University of Jerusalem, Jerusalem, Israel 91904

Edited by John A. Rogers, Northwestern University, Evanston, IL, and approved March 23, 2020 (received for review November 17, 2019)

Problems of flexible mechanical metamaterials, and highly deformable porous solids in general, are rich and complex due to their nonlinear mechanics and the presence of nontrivial geometrical effects. While numeric approaches are successful, analytic tools and conceptual frameworks are largely lacking. Using an analogy with electrostatics, and building on recent developments in a nonlinear geometric formulation of elasticity, we develop a formalism that maps the two-dimensional (2D) elastic problem into that of nonlinear interaction of elastic charges. This approach offers an intuitive conceptual framework, qualitatively explaining the linear response, the onset of mechanical instability, and aspects of the postinstability state. Apart from intuition, the formalism also quantitatively reproduces full numeric simulations of several prototypical 2D structures. Possible applications of the tools developed in this work for the study of ordered and disordered 2D porous elastic metamaterials are discussed.

mechanical metamaterials | elastic charges | nonlinear elasticity

The hallmark of condensed-matter physics, as described by P. W. Anderson in his paper "More is different" (1), is the emergence of collective phenomena out of well-understood simple interactions between material elements. Within the ever-increasing list of such systems, mechanical metamaterials form a particularly interesting class due to the high contrast between the simplicity of the interactions between constituting elements and the richness of the emergent physics (2–4).

While initial studies focused on the design of mechanical metamaterials with unusual mechanical properties in the linear regime (2, 3), more recently it has been shown that by embracing large deformations and instabilities these systems can achieve exotic functionalities (4). A prominent example of such nonlinear mechanical metamaterials consists of an elastomeric matrix with an embedded periodic array of holes (5). A typical stress–strain curve for such two-dimensional (2D) elastic metamaterials is shown in Fig. 1*A*. Under uniaxial compression, the linear response of the solid (at small loads) is a uniform deformation of the circular holes into ellipses, with their major axes oriented perpendicular to the direction of compression (see, e.g., Fig. 4, *Right*). This deformation is typically difficult to see experimentally, because at higher loads the system develops an instability and the stress plateaus. In a square lattice this instability results in the formation of a checkerboard pattern with the elongated holes taking alternate horizontal and vertical orientations, whereas in triangular lattices it leads to either a "zig-zag" or a Rosetta pattern (Fig. 1*C*), depending on the direction of the load. This spontaneous breaking of symmetry is a telltale sign of an underlying nonlinear mechanism responsible for an instability (6). Interestingly, this response is largely material independent, not only qualitatively but also quantitatively (e.g., the critical strain at instability), implying a universal origin of the nonlinear mechanism. A central question then is how the nontrivial mechanics of these perforated elastic metamaterials emerge from their underlying elasticity.

A theoretical analysis of the elastic problem requires solving the nonlinear equations of elasticity while satisfying the multiple free boundary conditions on the holes' edges—a seemingly hopeless task from an analytic perspective. However, direct solutions of the fully nonlinear elastic equations are accessible using finite-element models, which accurately reproduce the deformation fields, the critical strain, and the effective elastic coefficients, etc. (6). The success of finite-element (FE) simulations in predicting the mechanics of perforated elastic materials confirms that nonlinear elasticity theory is a valid description, but emphasizes the lack of insightful analytical solutions to the problem.

A first attempt toward a theoretical explanation for this phenomenon was taken by Matsumoto and Kamien (7, 8), who studied the interactions between holes based on the linear theory of elasticity. In their works they showed that the buckled patterns are consistent with energy-minimizing configurations of interacting holes, if each hole is modeled as a pair of dislocations. While their work successfully captures the buckled modes, this approach is qualitative and cannot predict either the critical strain at instability or the preinstability linear response and the effects of holes on it. However, as a theory limited to describing the buckled state, Matsumoto and Kamien's (7, 8) success implies that the concept of interacting holes can form the basis

Significance

Elastic metamaterials—stretchable solids with an engineered micropattern of holes and ligaments—form an important class of matter due to their unusual, and tunable, mechanical properties. Understanding how the hole structure affects the emergent mechanical response, i.e., developing a predictive theory of elastic metamaterials, is a problem of great significance, both as a fundamental scientific question and as an engineering challenge regarding design of novel structures and optimization of existing ones. Combining ideas from electrostatics with a modern theory of geometrical elasticity we develop an intuitive and quantitatively accurate conceptual formalism, which maps the elastic problem into that of nonlinearly interacting charges. This approach for tackling the problem naturally allows importing powerful techniques from statistical mechanics and dynamical systems.

Author contributions: Y.B.-S., K.B., and M.M. designed research; Y.B.-S., G.L., K.B., and M.M. performed research; M.M. contributed new reagents/analytic tools; Y.B.-S., G.L., and M.M. analyzed data; and Y.B.-S. and M.M. wrote the paper.

The authors declare no competing interest.

This article is a PNAS Direct Submission.

Data deposition: All numerical data discussed in this paper, as well as a *Mathematica* notebook that contains a detailed derivation of the theoretical results, are available to the reader on GitHub at https://github.com/yohai/elastic_charges_metamaterials.

[1]To whom correspondence may be addressed. Email: michael.moshe@mail.huji.ac.il.

This article contains supporting information online at https://www.pnas.org/lookup/suppl/doi:10.1073/pnas.1920237117/-/DCSupplemental.

First published April 29, 2020.

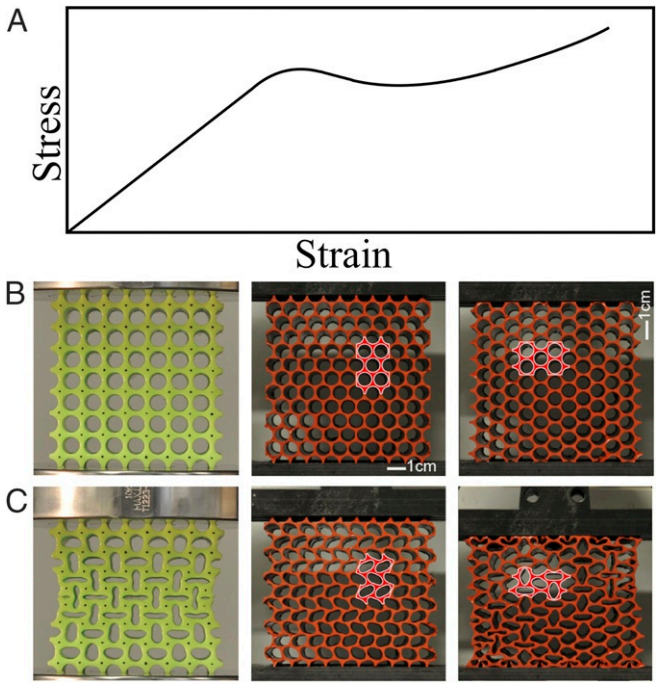

Fig. 1. (*A*) A sketch of a typical stress–strain curve for periodically perforated elastic metamaterial. (*B* and *C*) Metamaterials composed of an elastomer with a square lattice (*Left* column) or triangular lattices at two different orientations (*Center* and *Right* columns). The materials are shown in undeformed (*B*) and postbuckling deformed (*C*) configurations, under uniaxial compression. In the square lattice the instability is reflected as a checkerboard pattern of horizontal and vertical hole shapes whereas in the triangular lattice, due to frustration, the unstable mode forms either a zig-zag or a Rosetta pattern, depending on the direction of loading.

for an effective "lattice" theory of elastic metamaterials with periodic arrays of holes.

In this work we derive a formalism that bridges the gap between the successful "microscopic theory" (nonlinear elasticity) and the macroscopic effective theory. As we will show, this formalism provides an insightful and intuitive description of perforated elastic metamaterials without losing the quantitative capabilities of the microscopic theory. While the algebra might be somewhat technical, the qualitative picture that emerges from it is clean and elegant. Therefore, we structure the paper as follows: First, we qualitatively derive the main results of our analysis, using an analogy to a well-known problem in electrostatics (*Qualitative Picture*). Then, we describe the full formalism (*The Method*) and finally we quantitatively compare its predictions to full numerical calculations (*Results*).

Qualitative Picture

There are two major challenges in writing an analytical theory: the multiple boundary conditions imposed by the holes and the nonlinearity. As shown below, both these challenges can be tackled with the language of singular elastic charges. In what follows we demonstrate that the phenomena can be approximately, but quantitatively, described in terms of interacting elastic charges with quadrupolar symmetry, located at the center of each hole. These are image charges, much like the image charges that are used to solve simple electrostatic problems (9). When the loading is weak (linear response), the interaction of the charges with the external field dominates and the quadrupoles align perpendicularly to the direction of compression. At higher stresses, due to geometrical nonlinearities, the interaction between charges dominates their interaction with the external field, leading to the buckling instability that creates the patterns shown in Fig. 1.

Using the language of singular image charges to simplify calculations is common in field theories governed by the Laplace (or bi-Laplace) equation. Besides the well-known electrostatic example, this technique was used in analyzing low Reynolds number fluid dynamics (refs. 10–14, among many others), flux pinning in superconductors (15), capillary action (16), linear elasticity (17, 18), and relativity (19). Below we use the language of electrostatics, which we assume is familiar to the reader, to give a pedagogical analogy for the corresponding problem in elasticity.

Electrostatic Analogy. Consider a circular conductive shell in the presence of a uniform external electric field. Solving for the resultant field requires a solution of Laplace's equation with specific boundary conditions on the conductive surface. One particularly insightful method to solve this equation, introduced in elementary physics classes, is the method of image charges. The trick is that placing "imaginary" charges outside the domain of interest (i.e., inside the shell) solves by construction the bulk equation, and wisely chosen charges can also satisfy the boundary conditions. Indeed, the problem is solved exactly by placing a pure dipole at the shell center. From the perspective of an observer outside the shell, the presence of the conductive surface is indistinguishable from that of a pure dipole. Thus, the concept of image charge not only opens an analytic pathway for solving the problem, but also provides intuition about the solution and specifically on the physical effect of boundaries.

We note two properties of the solution which will have exact analogs in elasticity: First, the imaginary charge is a dipole, not a monopole. Electrostatic monopole image charges are disallowed because they are locally conserved. That is, the net charge in a given region can be completely determined by a surface integral on the region's boundary (Gauss's theorem). Second, the magnitude of the dipole moment turns out to be proportional to the external field and to the circle's area (in 2D).

How are the correct image charges found? A common strategy is to find them by enforcing the boundary conditions directly. This works only in cases where the image charges can exactly solve the problem. An alternative approach is via energy minimization, which gives an approximate solution when the exact one cannot be represented by a finite number of image charges. In fact, a potential ϕ that satisfies the bulk equation and its boundary conditions is also a minimizer of the energy

$$F = \int_{\Omega} \tfrac{1}{2} |\vec{\nabla}\phi - \boldsymbol{E}^{ext}|^2 \mathrm{d}S - \oint_{\partial\Omega} \rho\, \phi\, \mathrm{d}l, \qquad [1]$$

where $\boldsymbol{E}^{ext}$ is the imposed external field, Ω is the problem domain (e.g., $\mathbb{R}^2$ with a circle taken out), and $\partial\Omega$ is its boundary. For simplicity, here we work in units where the permittivity of space is unity. The function ρ is a Lagrange multiplier enforcing a constant potential on the conducting boundary (*SI Appendix*). For the problem described above, after guessing a solution in the form of a single dipole, its magnitude can be found by minimizing the energy Eq. **1** with respect to the dipole vector and ρ. The result satisfies the boundary conditions exactly.

Consider now a harder problem: an array of conducting circular shells in an external electric field, introducing the complication of multiple boundary conditions. In contrast with the single-shell problem, guessing a finite number of image charges that will balance boundary conditions is impossible: The image charges are now reflections of the external field, but also of all other image charges. Therefore, in general, the image charge in each shell is composed of an infinite number of multipoles. While an exact solution is hard to guess, by minimizing the energy we can nonetheless obtain an approximate solution. Each circular

shell is going to be polarized, and the dominant image charge inside each shell is dipolar: While imaginary dipoles can balance uniform electric fields on a circle, higher-order multipoles correspond to balancing fields that vary spatially on the scale of the shell. Thus, guessing a solution in terms of dipoles reflects an assumption on the spatial variability of the fields, and accounting for higher-order multipoles inside each shell would improve the accuracy of the solution. Specifically, we guess an ansatz of the form

$$\phi(\mathbf{x}) = \sum_i \mathbf{p}_i \cdot \boldsymbol{\phi}_{\mathbf{p}}(\mathbf{x} - \mathbf{x}_i), \qquad [2]$$

where $\mathbf{p}_i$ is the image dipole vector located at $\mathbf{x}_i$ (the center of the ith conducting shell), and $\boldsymbol{\phi}_{\mathbf{p}}$ is the well-known solution for the potential of a single electric dipole. The energy can be written as a quadratic form in the unknown charges $\mathbf{p}_i$,

$$F = \sum_{i,j} \mathbf{M}_{ij}\mathbf{p}_i\mathbf{p}_j - \sum_i \mathbf{m}_i\mathbf{p}_i, \qquad [3]$$

where

$$\mathbf{M}_{ij} = \frac{1}{2}\int_\Omega \left(\vec{\nabla}\boldsymbol{\phi}_{\mathbf{p}}(\mathbf{x}-\mathbf{x}_i)\right)\left(\vec{\nabla}\boldsymbol{\phi}_{\mathbf{p}}(\mathbf{x}-\mathbf{x}_j)\right)\mathrm{d}S,$$
$$\mathbf{m}_i = \oint_{\partial\Omega} \boldsymbol{\phi}_{\mathbf{p}}(\mathbf{x}-\mathbf{x}_i)\rho_i(\mathbf{x})\mathrm{d}l. \qquad [4]$$

The matrix $\mathbf{M}$ quantifies interactions between image dipoles in different shells, and $\mathbf{m}$ quantifies interactions of these dipoles with the external field. Since the potential of a dipole is known in explicit analytical form, calculating $\mathbf{M}$ and $\mathbf{m}$ is a trivial task of integration[†]. Then, minimizing the energy Eq. **3** is straightforward.

The Elastic Problem. All of the above concepts can be translated, with some modifications, to elasticity theory. The linear elastic analog of the single conducting shell problem happens to be a famous example, solved by Inglis (20) in 1913: a circular cavity in an infinite 2D elastic medium, subject to remote stress. Mathematically, the problem amounts to solving the biharmonic equation for the Airy stress function and, like the electrostatic analog, the Inglis solution is equivalent to a pure imaginary elastic charge at the shell center (21, 22). The charge is a quadrupole and in the linear theory its magnitude is proportional to the applied stress and to the hole's area (*SI Appendix*, section 2). But what are elastic charges?

A geometric approach to elasticity (23) uncovers the mathematical nature of elastic charges. The physical quantity associated with elastic charges is Gaussian curvature; that is, a monopolar charge is a singular distribution of Gaussian curvature. As an example, consider a thin conical surface confined to the flat Euclidean plane. The stressed state of the flattened cone reflects a geometric incompatibility between the flat embedding space and the conical reference state. The incompatibility is quantified by the Gaussian curvature of the reference state, which in the case of a cone is a delta-function singularity at the apex (24, 25).

Since the Gaussian curvature of the reference state acts as a singular source of elastic fields, it can be interpreted as an elastic charge. In crystalline materials, the monopole singularity described above is manifested as a disclination (24, 25). A dipole of elastic charges, i.e., a pair of disclinations of equal and opposite magnitude, forms a dislocation (24). Finally, a quadrupolar charge, like the one which solves the circular hole problem, is realized as a dislocation pair with equal and opposite Burgers vectors, which in hexagonal lattices is known as the Stone-Wales defect (26). In the context of continuum theory the elastic quadrupole is known as an elliptic Eshelby inclusion, i.e., an irreversible deformation of a circular domain into an ellipse (27, 28). Another realization of a quadrupole is a force dipole applied locally to an elastic substrate, e.g., by adherent contractile biological cells (29).

Like in the electrostatic case, the fact that the lowest-order multipole that solves the hole problem is a quadrupole is a direct consequence of a conservation theorem. In electrostatics, local creation of monopoles is disallowed by conservation. In elasticity, both the monopole (Frank's vector) and the dipole (Burgers' vector) are conserved (30, 31). For a rigorous derivation of all these results, see ref. 32.

With the method of image charges on one hand and the concept of elastic charges on the other hand, we can now attack the problem of 2D elastic metamaterials containing an array of holes. This problem can be solved by placing imaginary charges in the center of each hole, but these charges also create their own image charges inside other holes, like in the electrostatic case of an array of conducting shells. That is, the complex interactions between holes can be described in terms of multiple image charges interacting with each other and with the imposed external field. As in the electrostatic case, an approximate solution for a given external load can be derived by guessing a solution for which the elastic fields are dominated by the lowest-order nontopological charges, that is, imaginary quadrupoles (22).

Interacting Quadrupoles. Let us assume for the moment that the solution is indeed composed of a quadrupole located at the center of each hole. As a first attempt, let us also assume that the magnitude of all quadrupoles is fixed and they are free to rotate (this is in fact a good approximation for the cases shown in Fig. 1 *B* and *C*, *Left* and *Center*). This picture, of interacting rotating quadrupoles, is very close in spirit to the phenomenological description in Matsumoto and Kamien (7), who described each hole as a pair of opposite dislocations, i.e., an elastic quadrupole. To proceed, we need to understand the interaction between two pure elastic quadrupoles in an infinite elastic medium. For two quadrupoles of magnitude Q_1, Q_2 and orientations θ_1, θ_2 (θ_i is measured with respect to the line connecting the two quadrupoles; Fig. 2*A*), the interaction energy is (33)

$$E = \frac{Q_1 Q_2}{\pi r}\cos(2\theta_1 + 2\theta_2). \qquad [5]$$

This energy is minimized for configurations satisfying $\theta_1 + \theta_2 = \pi/2$, which is a one-dimensional continuum of minimizers. Fig. 2*A* presents two such optimal configurations.

What is the optimal configuration of a lattice of quadrupoles? For a square lattice, if only nearest-neighbors interactions are taken into account, two distinct energy-minimizing configurations satisfy the condition $\theta_1 + \theta_2 = \pi/2$ for all neighboring quadrupoles: 1) all quadrupoles having an angle of $\pi/4$ relative to the horizontal axis (as in Fig. 2*A*, *Top*) and 2) a checkerboard pattern of horizontal and vertical quadrupoles (as in Fig. 2 *A* and *B*, *Bottom*). The checkerboard pattern has a lower energy because it also minimizes the interaction between quadrupoles on opposing sides of the unit square diagonal, i.e., next-nearest neighbors. Note that this is exactly the pattern of the buckled state of the square lattice (cf. Fig. 1).

Unlike the square lattice, the symmetries of the triangular lattice are incompatible with those of the interacting quadrupoles; i.e., it is impossible to simultaneously minimize the interaction of the quadrupoles with the external field and their nearest

[†]In principle, one should also decompose ρ in terms of the dipolar fields. We do not go into these details here.

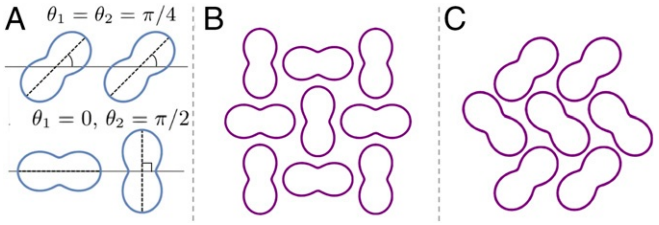

Fig. 2. Interacting elastic quadrupoles, illustrated by the deformation fields they induce on the holes' edges. (*A*) Two energy-minimizing configurations of quadrupoles of fixed magnitudes and free orientations. *Top* configuration shows $\theta_1 = \theta_2 = \pi/4$ while *Bottom* one shows $\theta_1 = 0$, $\theta_2 = \pi/2$. (*B*) An array of quadrupoles on a square lattice minimizing their interaction energy with nearest and next to nearest neighbors, as given by Eq. **5**. The relative orientation of any nearest-neighbor pair is like that in *A*, *Bottom*, and that of next-nearest pairs is like that in *A*, *Top*. (*C*) Like *B*, but for a triangular lattice.

neighbors. Direct minimization of nearest-neighbors interactions energy with respect to quadrupoles orientations gives the pattern shown in Fig. 2*C*. As before, the quadrupole orientations are in agreement with the observed unstable mode. The Rosetta pattern observed in Fig. 1*C*, *Right*, however, is not captured by this simplified model, since in it the quadrupole magnitudes are not uniform.

Collecting the Pieces. The conclusion from the previous section is that the unstable modes resemble a collection of interacting quadrupoles. We suggest that rigorously describing the system as a collection of interacting quadrupoles is a perturbative approximation of the full solution: At low stresses, all quadrupoles are aligned with the external field. At higher stresses the elastic metamaterial buckles and, as we have just seen, the buckled states are consistent with a model of interacting quadrupoles. This suggests that the postinstability response is dominated by charge–charge interaction rather than interactions of charges with the external load.

We emphasize, however, that this picture does not have a (linear) electrostatic analog. In linear systems, the induced charges are always proportional to the external loading (E^{ext} in Eq. **1**) and therefore the interaction between themselves cannot, by construction, dominate their interaction with the external field. The mechanism described above is manifestly nonlinear and requires a generalization of the electrostatic arguments. The observed instability emerges from a geometric nonlinearity, which is inherent to elasticity and does not have an electrostatic analog. Below we show how the framework of interacting charges can be expanded to account for all these effects.

The Method

The fundamental field in the theory of elasticity is the displacement field $\mathbf{d}$, which measures the spatial movement of material elements from a reference position to its current one. Local length deformations are quantified by the strain tensor $\mathbf{u}$ (34),

$$\mathbf{u} = \frac{1}{2}\left(\nabla\mathbf{d} + \nabla\mathbf{d}^T + \nabla\mathbf{d}^T \cdot \nabla\mathbf{d}\right). \quad [6]$$

The elastic energy density, which results from local length changes, can be written as a function of $\mathbf{u}$. Linear elasticity is a leading-order perturbation theory for small deformations and therefore E is written as a quadratic function of $\mathbf{u}$, alias Hookean energy

$$E = \langle \mathbf{u}, \mathbf{u} \rangle + \mathcal{O}(\mathbf{u}^3). \quad [7]$$

Here $\langle \mathbf{v}, \mathbf{u} \rangle \equiv \int_\Omega \frac{1}{2}\mathbf{v}\mathcal{A}\mathbf{u}\, \mathrm{d}S$ is an integration over the domain Ω of the contraction of the tensor fields $\mathbf{u}, \mathbf{v}$ with a 4-rank tensor $\mathcal{A}$, known as the elastic (or stiffness) tensor, which encodes material properties such as Young's modulus and Poisson's ratio (*SI Appendix*, Eq. **S4**).

Although the energy is quadratic, the theory as presented above is still nonlinear due to the $\nabla\mathbf{d}^T \cdot \nabla\mathbf{d}$ term in strain (Eq. **6**). Neglecting it (assuming $\nabla\mathbf{d} \ll 1$) yields the familiar theory of linear elasticity (30). That is, linear elasticity is obtained by performing two conceptually distinct linearizations: a rheological linearization, neglecting higher-order material properties (the $\mathcal{O}(\mathbf{u}^3)$ term in Eq. **7**), and a geometrical linearization, neglecting the quadratic term in Eq. **6**. In the former, the neglected nonlinear behavior is rheological and therefore material specific. In the latter, the neglected terms are geometrically universal and relate to rotational invariance. Since, as described above, the nonlinear mechanics of elastic metamaterials with arrays of holes are largely material independent, it is reasonable to speculate that a suitable analytical description of the system is that of a nonlinear geometry with a quadratic (Hookean) energy. Therefore, we take Eqs. **6** and **7** to be the governing equations in this work.

Numerical analysis has confirmed the applicability of these equations in two respects: First, a full numerical solution of the governing equations accurately reproduces experimental results (6). Second, calculations show that even in the buckled state, which is clearly a nonlinear response, $|\nabla\mathbf{d}|$ is of order unity[‡] due to almost-rigid rotations of the junctions between holes, invalidating the geometric linearization. However, the nonlinear strain, Eq. **6**, is small due to cancelation of the linear and quadratic terms, justifying the rheological linearization in Eq. **6**. From a theoretical perspective this observation suggests that a careful analysis of small nonlinear strains should recover the phenomenology of perforated elastic metamaterials.

Bulk Energy. Similarly to Eq. **2**, we express the total deformation in the system as induced by quadrupoles located at the centers of the holes, with some charges placed in lattice sites immediately outside the solid, as illustrated in Fig. 3. Using a recent generalization of the method of Airy stress function, which allows solving elastic problems with arbitrary constitutive relations, strain definitions, or reference states (33, 35), we perform a perturbative expansion of the nonlinear quadrupolar fields[§]. Symbolically, the displacement induced by a single charge $q_{\alpha\beta i}$ located at $\mathbf{x}_i$ is expanded in powers of charges

$$\mathbf{d}(\mathbf{x}) = \sum_{i,\alpha,\beta} q_{\alpha\beta i}\, \mathbf{d}^{(1)}_{\alpha\beta}(\mathbf{x} - \mathbf{x}_i) + {q_{\alpha\beta i}}^2\, \mathbf{d}^{(2)}_{\alpha\beta}(\mathbf{x} - \mathbf{x}_i) + \mathcal{O}(q^3), \quad [8]$$

where $\mathbf{d}^{(n)}_{\alpha\beta}$ is the displacement to the nth order associated with the charge $q_{\alpha\beta i}$. Here Greek indices represent the different quadrupolar components and Latin indices represent the location of the image charge in the 2D lattice. A detailed derivation is given in *SI Appendix*, section 1 and explicit analytical forms of the geometrically nonlinear fields associated with small elastic multipolar charges are given in an attached *Mathematica* notebook (see Data Availability for details). In addition to image charges at the hole centers, we also allow for uniform elastic fields, which within the formalism are described as quadrupolar charges located at infinity.

[‡]e.g., with respect to the Frobenius norm.

[§]In fact, a careful analysis of the elastic equations reveals that there are two distinct types of elastic monopoles and consequently also two types of quadrupoles. For succinctness in the text we refer to quadrupoles in a general manner, but in the actual calculations we do take into account both types of quadrupoles in each hole. A detailed calculation is presented in *SI Appendix*.

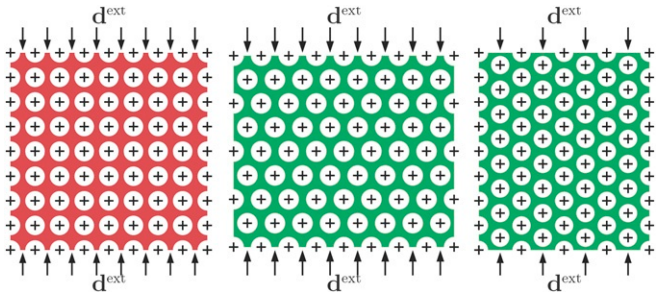

Fig. 3. The three prototypical lattices studied in this work. Shown are square and triangular lattices of circular holes with uniform size subjected to external displacement $\mathbf{d}^{\text{ext}}$ applied on the ligaments forming the boundaries. The locations of the image charges are marked with black + signs. The ligaments over which the displacement boundary conditions are imposed are marked with arrows.

We note that Eq. **8** contains two distinct approximations: 1) truncating the multipole expansion at the quadrupolar order and 2) truncating the expansion at the quadratic order in q. The former is an uncontrolled approximation whose validity depends on the geometry of the system, and the latter is a controlled approximation, which becomes exact in the limit of small (nonlinear) strains (32).

For notational simplicity, it is easier to denote the collection of all components of all charges, either at hole centers or at infinity, by a single vector $\mathbf{Q}$, replacing the three indices α, β, i by a single index. Combining the ansatz Eq. **8** with the elastic energy Eqs. **6** and **7**, we obtain

$$E = \sum_{ij} \mathcal{M}^{(2)}_{ij}\, Q_i\, Q_j + \sum_{ijk} \mathcal{M}^{(3)}_{ijk}\, Q_i\, Q_j\, Q_k + \dots, \qquad [9]$$

where

$$\begin{aligned} \mathcal{M}^{(2)}_{ij} &= \left\langle \mathbf{u}^{(1)}_i, \mathbf{u}^{(1)}_j \right\rangle \\ \mathcal{M}^{(3)}_{ijk} &= \left\langle \mathbf{u}^{(1)}_i, \mathbf{u}^{(2)}_j \right\rangle \delta_{jk} + \left\langle \mathbf{u}^{(2)}_i, \mathbf{u}^{(1)}_j \right\rangle \delta_{ik}. \end{aligned} \qquad [10]$$

Here, $\mathbf{u}^{(k)}_j$ is the strain field derived from the displacement field $\mathbf{d}^{(k)}_j$ induced by the image charges and δ_{ij} is the Kronecker delta. Note that no summation is implied in Eq. **10**.

The matrix $\mathcal{M}^{(2)}$, similar to the electrostatic analog $\mathbf{M}$ of Eq. **4**, has a simple interpretation: It is a positive-definite matrix that quantifies pair interactions between charges, taking into account their relative position and the geometry of the domain. Similarly, $\mathcal{M}^{(3)}$ describes the interactions between triplets of charges, and so on.

Calculating the interaction matrices $\mathcal{M}$ involves integration of explicitly known expressions over the perforated domain. One could attempt to analytically calculate these integrals under some approximations (i.e., keeping only nearest-neighbor interactions), which is the subject of future research. In this work, to strictly test the elastic-charges approach and avoid additional approximations, we evaluate the integrals numerically.

External Loading. In the electrostatic example above we dealt with infinite systems where the external loading was imposed by a bulk energetic term ($\boldsymbol{E}^{ext}$ in Eq. **1**). It is possible to include such a term in the elastic theory too, but in this work we want to analyze the case most commonly encountered in reality: a finite system with displacement-controlled boundary conditions, as in Fig. 1. This requires a different approach and there are a few ways in which these boundary conditions can be introduced within our formalism. We found that, in the context of the lattice–hole geometry, imposing boundary conditions on the external edges is most conveniently done by treating the boundary conditions as constraints on the unknown charges $\mathbf{Q}$.

As discussed above, the boundary conditions cannot be satisfied exactly when expressing the relevant fields with a finite number of charges. However, an approximate solution can be obtained by demanding that the boundary conditions will be satisfied on average in a particular region. Consider the geometry of the system, depicted in Fig. 3: The top and bottom boundaries of the lattice are loaded by a rigid plate. The actual contact points between the system and the loading mechanism are a discrete set of ligaments, marked with arrows in Fig. 3. Focusing on one of them, the average displacement on the boundary is given by

$$\bar{\mathbf{d}} = \sum_i \mathcal{N}^{(1)}_i\, Q_i + \mathcal{N}^{(2)}_i\, {Q_i}^2 + \cdots, \qquad [11]$$

where $\mathcal{N}^{(i)}$ can be expressed by explicit integration of Eq. **8** over the ligament (*SI Appendix*, section 4). Imposing a given average displacement on a set of ligaments translates to a collection of nonlinear constraints on the charges, one for each ligament. That is, the constraints on the charges are

$$\left(\sum_i Q_i \mathcal{N}^{(1)}_{ij} + {Q_j}^2 \mathcal{N}^{(2)}_{ij} + \cdots \right) - \mathbf{d}^{ext}_j = 0, \qquad [12]$$

where $\mathbf{d}^{ext}_j$ is the imposed displacement on the jth ligament and $\mathcal{N}^{(i)}$ is an $N \times c$ matrix. Here, c is the number of constraints and N is the number of charge components, i.e., the length of the vector $\mathbf{Q}$.

In this formalism, finding the charges that best approximate the boundary conditions amounts to minimizing the nonlinear energy Eq. **9** under the nonlinear constraints of Eq. **12**.

Results

Here we use the method of image quadrupoles to analyze three situations, shown in Fig. 3: a square lattice and a triangular lattice compressed along two different orientations. The square and triangular lattices contain 81 and 77 holes, respectively, and are characterized by their porosity, defined as the fractional area of holes. Here we analyze systems with porosity that ranges from $p = 0.3$ to $p = 0.7$ (the percolation limit is at $p \approx 0.78$ for the square lattice and $p \approx 0.90$ for the triangular one). To test the theory we compare our results with direct numeric simulations of the full equations, which are known to agree very well with experiments (6). In both analysis and simulations we leave no fitting parameters, and we use the same elastic moduli ($Y = 1$ is the 2D Young's modulus and $\nu = 1/3$ is the 2D Poisson's ratio).

Linear Response. We begin by analyzing the linear response of the system under small displacements. In this limit, only the leading-order contributions are considered. That is, we minimize the quadratic energy $E = \sum_{ij} \mathcal{M}^{(2)}_{ij}\, Q_i\, Q_j$ under the set of linear constraints $\sum_j \mathcal{N}^{(1)}_{ij} Q_j = \mathbf{d}^{ext}_i$. This is a trivial exercise in linear algebra, and the desired charges are given by (*SI Appendix*, section 4)

$$\mathbf{Q}^* = -\mathcal{M}^{-1}\mathcal{N}\left(\mathcal{N}^T\mathcal{M}^{-1}\mathcal{N}\right)^{-1}\mathbf{d}^{ext}, \qquad [13]$$

where for ease of notation we omitted the superscripts $\mathcal{M} \equiv \mathcal{M}^{(2)}$ and $\mathcal{N} \equiv \mathcal{N}^{(1)}$. With $\mathbf{Q}^*$, the solution can be written in terms of Eq. **8** and any property of interest can be extracted. For example, the effective Young's modulus Y_{eff} can be easily obtained in closed form; see derivation in *SI Appendix*, section 4A. In Fig. 4, *Left* column, we plot Y_{eff} as function of porosity, measuring the system's compliance for uniaxial loads, i.e., its

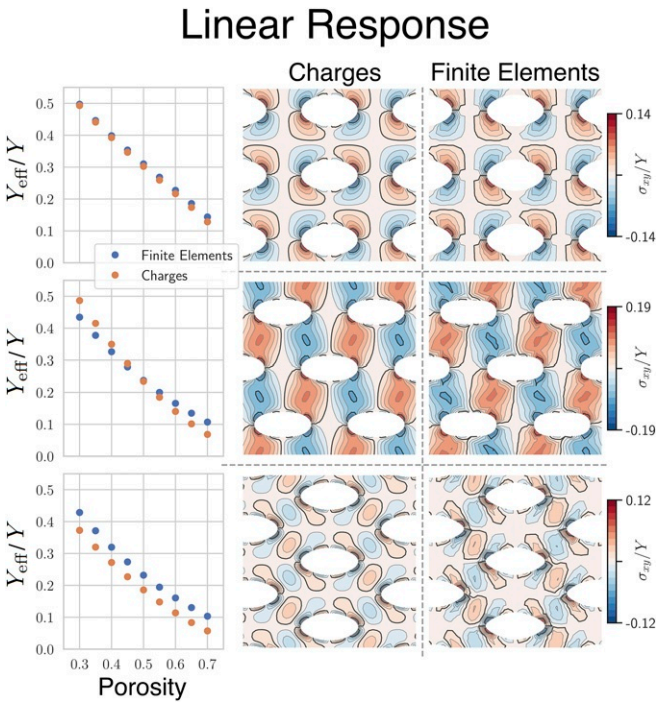

Fig. 4. Comparison between the elastic-charges calculation and a direct fully nonlinear numerical solution in the linear regimes for three different lattices. *Left* column shows the effective Young's modulus as function of porosity (blue for finite element, orange for elastic charges). Each point represents the slope in the stress–strain curve of a system with the corresponding hole pattern and porosity. *Center* and *Right* columns show representative fields of the σ^{xy} component of the stress-field distribution plotted on top of the strained configurations with porosity $p = 0.3$.

effective spring constant. It is defined by the ratio of the average compressive stress to the compressive strain. Comparison to direct numerical simulations shows that the formalism quantitatively captures the coarse-grained response of the system. In addition, in Fig. 4, *Center* and *Right* columns we plot the spatial distribution of the shear stress field σ^{xy} for a representative porosity and imposed strain, plotted on top of the deformed configurations, showing a favorable agreement also in the detailed spatial structure of the solution. We emphasize that the charge formalism has no free parameters to fit.

A slight discrepancy in the deformation field is observed in one orientation of the triangular lattice, as shown in Fig. 4, *Bottom* row, reflecting the fact that quadrupolar charges cannot fully describe the solution. To capture these details, higher-order multipoles are needed.

Instability (Nonlinear Response). Encouraged by the success of the image charge method in the linear regime, we now proceed to study the nonlinear instability of the system. In particular, we are interested in the critical strain at the onset of instability and the unstable modes.

The stability of the system is determined by the Hessian of the energy which in the linear response regime is simply $2\mathcal{M}^{(2)}$. It is guaranteed to be positive definite and the system is thus stable. Expanding to the next order in $\mathbf{d}^{ext}$, we find that the Hessian reads

$$H_{ij} = 2\mathcal{M}^{(2)}_{ij} + 2Q^*_k \left[\mathcal{M}^{(3)}_{ijk} + \mathcal{M}^{(3)}_{ikj} + \mathcal{M}^{(3)}_{kij}\right], \qquad [14]$$

where no summation is intended on i and j. In addition, the displacement constraints of Eq. **12** should also be corrected to next-leading order. This technical calculation is done in detail in *SI Appendix*, section 4B.

The charges in the linear solution, $\mathbf{Q}^*$, are proportional to the imposed displacement $\mathbf{d}^{ext}$; cf. Eq. **13**. This means that the leading-order correction to the Hessian (the bracketed term in Eq. **14**), as well as the correction to the displacement constraints, is also linear in $\mathbf{d}^{ext}$. When the imposed displacement is large enough, the constrained Hessian can become singular; i.e., one of its eigenvalues can vanish. This is the onset of instability.

We note that this calculation is in line with the intuitive picture described above: For small loads (i.e., in the linear regime) the dominant interaction is that of the charges with the external loading and with themselves, quantified respectively by $\mathcal{N}^{(1)}$ and $\mathcal{M}^{(2)}$. In this regime the solution is linear in $\mathbf{d}^{ext}$ and given by Eq. **13**. It is stable because $\mathcal{M}^{(2)}$ is positive definite. For larger loads, the interaction of the induced charges with themselves, quantified by $\mathcal{M}^{(3)}$, becomes important and eventually destabilizes the linear solution.

Fig. 5, *Left* column shows the critical strain, i.e., the strain at which the Hessian becomes singular, as a function of porosity for the three different lattices. Our method is in good quantitative agreement with the full numerical simulations, except possibly at very low porosities. This happens because smaller porosities lead to larger critical strains, making the image charge magnitudes larger. Because our method is a perturbative expansion in the charge magnitude, its accuracy deteriorates when the charges are large. This effect is more noticeable in the triangular lattices (Fig. 5, *Middle* and *Bottom* rows).

For each lattice, we also plot the unstable eigenmode associated with the vanishing eigenvalue. Representative ones are plotted in Fig. 5, *Center Left* and *Center Right* columns. In two of the three cases shown, the unstable modes computed with our method agree with those found in finite-element simulations. In the case shown in Fig. 5, *Middle* row, there is a discrepancy, which might come as a surprise because the formalism properly identifies the critical strain, i.e., the load where a specific eigenmode becomes unstable, while the mode itself is not the right one. A deeper investigation reveals that many eigenmodes become unstable almost simultaneously, making it difficult to pinpoint the least stable one. This is clearly seen in Fig. 5, *Right* column, where at the onset of instability many eigenvalues are densely distributed close to the vanishing one. The zig-zag–like mode, like the one predicted by finite-element simulations and by the interacting quadrupole model of Fig. 2, also becomes unstable at a similar strain. While we are still not sure about the precise origin of this inconsistency, we suspect that it is rooted in the difficulty of satisfying the boundary condition on the external boundary of the solid, i.e., a finite-size effect.

Summary and Discussion

We introduced a formalism that identifies image elastic charges as the basic degrees of freedom of perforated elastic metamaterials. The continuum elastic problem, which contains multiple boundary conditions, is reduced to a simpler problem of a lattice of nonlinearly interacting elastic quadrupoles.

While the focus of our work is on 2D elastic metamaterials, the concept of image charges is applicable in principle in any dimension, although its implementation may be rather complicated. For example, elastic charges are defined as singularities of a curvature field. In 2D the curvature is a scalar, introducing a significant level of simplicity. In higher dimensions curvature is no longer a scalar but a tensor, and in 3D elastic charges are singularities of a second-rank tensor field (the reference Ricci curvature). Generalizing our theory to 3D elastic metamaterials requires a classification of 3D elastic charges and calculation of their resulting elastic fields, a subject of ongoing research.

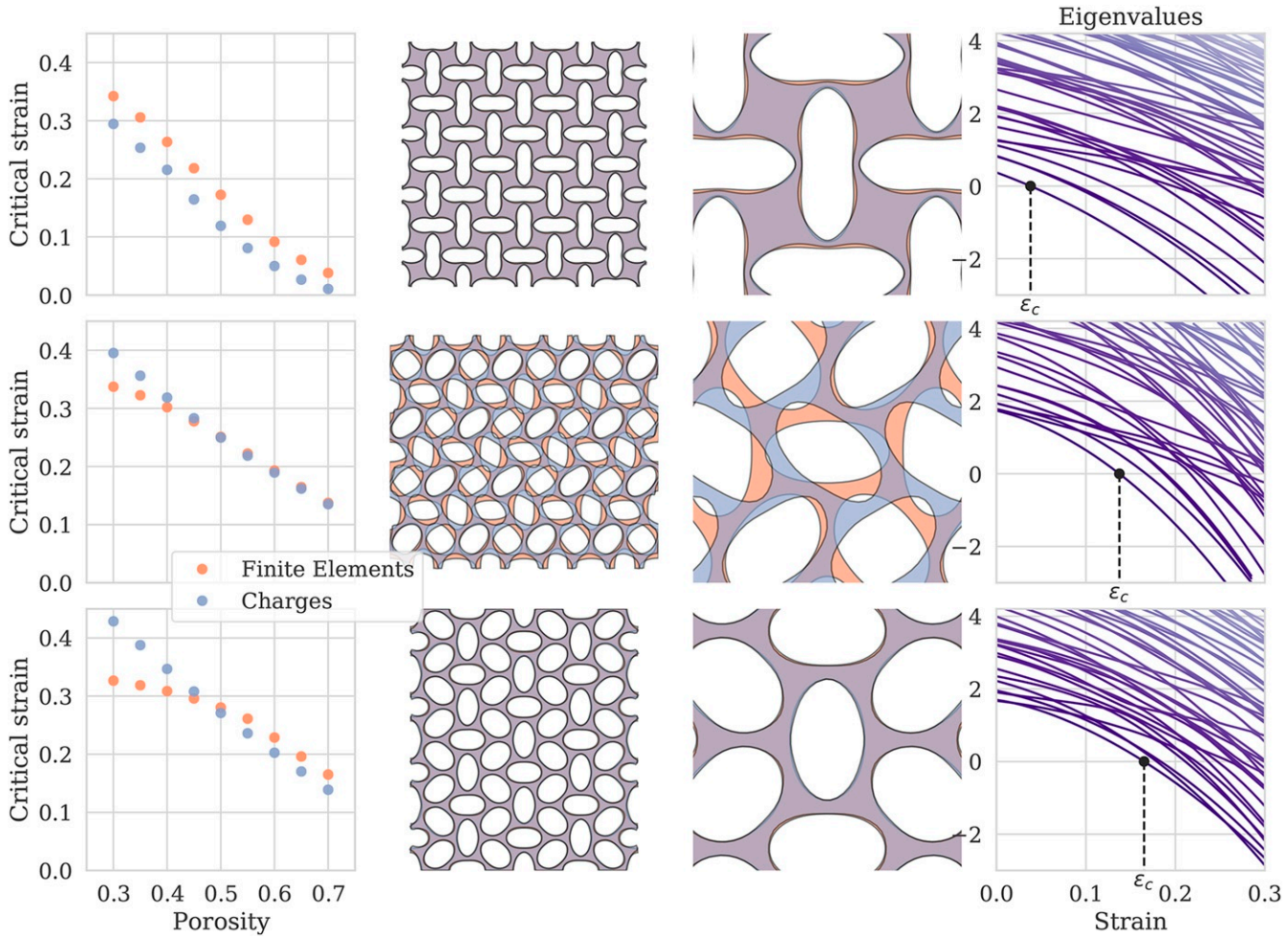

Fig. 5. Comparison between the elastic-charges calculation and a direct fully nonlinear numerical solution at the onset of instability for three different lattices. *Left* column plots the critical strain as function of porosity (orange for finite element, blue for elastic charges). *Center Left* and *Center Right* columns show the unstable modes for the whole system and a close-up of the *Center Left* column, respectively (same color code as *Left* column). These are all with porosity $p = 0.7$. *Right* column plots the eigenvalues as function of strain, demonstrating the formation of instability and the densely distributed vanishing eigenvalues at the onset of instability.

A central advantage of the elastic-charges approach is its conceptual aspect, in that it offers understanding and intuition about the deformation patterns before making any calculation. Both the linear response pattern and the buckled state can be qualitatively understood easily, as well the instability mechanism.

In addition, we found very good quantitative agreement between our theory and a detailed nonlinear finite-element analysis. This includes the effective Young's modulus, the stress-field distribution, the critical loads at the onset of instability, and the unstable modes. While some of the approximations we made are uncontrolled—namely truncating the multipolar expansion at the quadrupolar order and placing image charges only in the immediate vicinity of the finite solid as in Fig. 3—the quantitative agreement between our approach and the exact numeric results is a direct validation of our formalism, demonstrating a posteriori that, at least for the analyzed cases, multipoles higher than the quadrupoles may be neglected.

Finally, the charge formalism is also beneficial from a computational perspective, since it vastly reduces the number of degrees of freedom in the problem. For a finite-element simulation to be reliable, the mesh must contain at least a few dozen points per hole. In the simulations reported in this work, a reasonable accuracy demanded around 10^4 mesh points. The elastic charge formalism, on the other hand, requires a handful of degrees of freedom per hole. In the calculations reported here, we used the number 5, leading to $\sim 10^2$ degrees of freedom per lattice. All of the charge method calculations in this work combined can be run on a standard laptop within a matter of minutes.

However, we emphasize that in its present form, the model cannot serve as an alternative to the detailed finite-element analysis. For example, while our theory correctly describes mechanical properties prior to and at the onset of instability, it is not valid beyond the instability: Since our theory expands the energy only to third order, the postinstability energy does not have a minimum. Analyzing the postinstability response requires going to the next order, with a quartic energy functional. Then, identifying the energy-minimizing configuration corresponds to solving a set of cubic algebraic equations for the unknown charges, a task that we have found nontrivial and is a work in progress.

Looking forward, we suggest that this approach might open the way for importing techniques and ideas from statistical mechanics to the study of perforated elastic metamaterials. For example, we are currently investigating the effect of structural disorder by introducing randomness to the mechanical interactions between the charges (i.e., randomness in the interaction matrices $\mathcal{M}$ and $\mathcal{N}$). Another direction, for future work, would be coarse graining the model to develop a field theory where the quadrupolarization is a continuous field. This would be the analog of dielectric

materials described by distributing induced electric dipoles, but with a richer response.

Theoretical and Finite-Elements Method. The commercial software Abaqus/Standard was used for our FE simulations. Each mesh was constructed using six-node, quadratic, plane-stress elements (ABAQUS element type CPS6) and the accuracy was checked by mesh refinement. The material was modeled as an isotropic linear elastic material with 2D Poisson's ratio $\nu = 0.3$ and 2D Young's modulus $Y = 1$. In all our analyses the models were loaded by imposing a displacement d^{ext} to the two opposite horizontal edges, while leaving the vertical one traction-free (Fig. 3). To characterize the linear response, we conducted a static analysis assuming small deformations (*STATIC step with NLGEOM=OFF in Abaqus) and defined Y_{eff} as the slope of the resulting stress–strain curve. To characterize the critical strain, we conducted a buckling analysis on the undeformed configuration (*BUCKLE step in Abaqus).

Data Availability. All numerical data discussed in this paper, as well as a *Mathematica* notebook that contains a detailed derivation of the theoretical results, are available to the reader on GitHub at https://github.com/yohai/elastic_charges_metamaterials.

ACKNOWLEDGMENTS. M.M. acknowledges useful discussion with David R. Nelson, Mark J. Bowick, and Eran Sharon. Y.B.-S. acknowledges support from the James S. McDonnell postdoctoral fellowship for the study of complex systems. M.M. acknowledges support from the Israel Science Foundation (Grant 1441/19). K.B. acknowledges support from NSF Grants DMR-1420570 and DMR-1922321.

1. P. W. Anderson, More is different. *Science* **177**, 393–396 (1972).
2. M. Kadic, T. Bückmann, R. Schittny, M. Wegener, Metamaterials beyond electromagnetism. *Rep. Prog. Phys.* **76**, 126501 (2013).
3. J. Christensen, M. Kadic, O. Kraft, M. Wegener, Vibrant times for mechanical metamaterials. *MRS Commun.* **5**, 453–462 (2015).
4. K. Bertoldi, V. Vitelli, J. Christensen, M. van Hecke, Flexible mechanical metamaterials. *Nat. Rev. Mater.* **2**, 17066 (2017).
5. T. Mullin, S. Deschanel, K. Bertoldi, M. C. Boyce, Pattern transformation triggered by deformation. *Phys. Rev. Lett.* **99**, 084301 (2007).
6. K. Bertoldi, P. M. Reis, S. Willshaw, T. Mullin, Negative Poisson's ratio behavior induced by an elastic instability. *Adv. Mater.* **22**, 361–366 (2010).
7. E. A. Matsumoto, R. D. Kamien, Elastic-instability triggered pattern formation. *Phys. Rev.* **80**, 021604 (2009).
8. E. A. Matsumoto, R. D. Kamien, Patterns on a roll: A method of continuous feed nanoprinting. *Soft Matter* **8**, 11038–11041 (2012).
9. J. D. Jackson, *Classical Electrodynamics* (John Wiley & Sons, 2007).
10. G. Batchelor, *An Introduction to Fluid Dynamics* (Cambridge University Press, 2000).
11. J. Blake, A note on the image system for a stokeslet in a no-slip boundary. *Math. Proc. Camb. Philos. Soc.*, **70**, 303–310.
12. P. J. Mucha, S. Y. Tee, D. A. Weitz, B. I. Shraiman, M. P. Brenner, A model for velocity fluctuations in sedimentation. *J. Fluid Mech.* **501**, 71–104 (2004).
13. G. Batchelor, J. T. Green, The hydrodynamic interaction of two small freely-moving spheres in a linear flow field. *J. Fluid Mech.* **56**, 375–400 (1972).
14. R. M. Höfer, J. J. Velázquez, The method of reflections, homogenization and screening for Poisson and Stokes equations in perforated domains. *Arch. Ration. Mech. Anal.* **227**, 1165–1221 (2018).
15. A. A. Kordyuk, Magnetic levitation for hard superconductors. *J. Appl. Phys.* **83**, 610–612 (1998).
16. L. Botto, E. P. Lewandowski, M. Cavallaro, K. J. Stebe, Capillary interactions between anisotropic particles. *Soft Matter* **8**, 9957–9971 (2012).
17. I. Bischofs, S. Safran, U. Schwarz, Elastic interactions of active cells with soft materials. *Phys. Rev.* **69**, 021911 (2004).
18. S. Sarkar, M. Cebron, M. Brojan, A. Kosmrlj, Elastic multipole method for describing linear deformation of infinite 2d solid structures with circular holes and inclusions. arXiv:1910.01632 (3 October 2019).
19. C. W. Misner, The method of images in geometrostatics. *Ann. Phys.* **24**, 102–117 (1963).
20. C. E. Inglis, Stresses in a plate due to the presence of cracks and sharp corners. *Trans. Inst. Naval Archit.* **55**, 219–241 (1913).
21. M. Moshe *et al.*, Kirigami mechanics as stress relief by elastic charges. *Phys. Rev. Lett.* **122**, 048001 (2019).
22. M. Moshe *et al.*, Nonlinear mechanics of thin frames. *Phys. Rev.* **99**, 013002 (2019).
23. E. Efrati, E. Sharon, R. Kupferman, Elastic theory of unconstrained non-Euclidean plates. *JMPS* **57**, 762–775 (2009).
24. S. H. Seung, D. R. Nelson, Defects in flexible membranes with crystalline order. *Phys. Rev. A* **38**, 1005–1018 (1988).
25. M. Moshe, I. Levin, H. Aharoni, R. Kupferman, E. Sharon, Geometry and mechanics of two-dimensional defects in amorphous materials. *Proc. Natl. Acad. Sci. U.S.A.* **112**, 10873–10878 (2015).
26. A. J. Stone, D. J. Wales, Theoretical studies of icosahedral C60 and some related species. *Chem. Phys. Lett.* **128**, 501–503 (1986).
27. J. D. Eshelby, The determination of the elastic field of an ellipsoidal inclusion, and related problems. *Proc. Math. Phys. Eng. Sci.* **241**, 376–396 (1957).
28. R. Dasgupta, H. G. E. Hentschel, I. Procaccia, Microscopic mechanism of shear bands in amorphous solids. *Phys. Rev. Lett.* **109**, 255502 (2012).
29. U. S. Schwarz, S. A. Safran, Physics of adherent cells. *Rev. Mod. Phys.* **85**, 1327 (2013).
30. L. D. Landau, E. Lifshitz, *Theory of Elasticity* (Elsevier, New York, NY, 1986), vol. 3, pp. 109.
31. J. P. Hirth, J. Lothe, T. Mura, *Theory of Dislocations* (American Society of Mechanical Engineers Digital Collection, 1983).
32. R. Kupferman, M. Moshe, J. P. Solomon, Metric description of defects in amorphous materials. *Arch. Ration. Mech. Anal.* **216**, 1009–1047 (2015).
33. M. Moshe, E. Sharon, R. Kupferman, Elastic interactions between two-dimensional geometric defects. *Phys. Rev.* **92**, 062403 (2015).
34. L. D. Landau, E. M. Lifschitz, *The Theory of Elasticity* (Pergamon, 1986).
35. M. Moshe, E. Sharon, R. Kupferman, The plane stress state of residually stressed bodies: A stress function approach. arXiv:1409.6594 (23 September 2014).